Electronic Supplementary Information

Moderate Oxidation Levels of Ru Nanoparticles Enhance Molecular Oxygen Activation for Cross-Dehydrogenative-Coupling Reactions *via* Single Electron Transfer

Mu Lin,[‡a] Lin-Xiu Dai,[‡a] Jun Gu,[‡a] Li-Qun Kang,[a] Yu-Hao Wang,[a] Rui Si,[b] Ze-Qiong Zhao,[a] Wen-Chi Liu,[a] Xuefeng Fu,[a] Ling-Dong Sun,*[a] Ya-Wen Zhang,*[a] Chun-Hua Yan*[a]

[a]Beijing National Laboratory for Molecular Sciences, State Key Laboratory of Rare Earth Materials Chemistry and Applications, PKU-HKU Joint Laboratory in Rare Earth Materials and Bioinorganic Chemistry, College of Chemistry and Molecular Engineering, Peking University, Beijing 100871, China.

[b]Shanghai Synchrotron Radiation Facility, Shanghai Institute of Applied Physics, Chinese Academy of Sciences, Shanghai 201204, China.

E-mail: yan@pku.edu.cn, ywzhang@pku.edu.cn, sun@pku.edu.cn

Contents

1. Synthesis, Characterization and Catalysis Study of Ru Nanoparticles

1.1 Chemicals used in the preparation of catalysts

RuCl$_3$ xH$_2$O (A.R., Sinopharm Chemical Reagent Co. Ltd.), sodium oxalate (Na$_2$C$_2$O$_4$, A.R., Beijing Chemical Works), poly-vinylpyrrolidone (PVP; Mw ~29,000, Sigma-Aldrich), formaldehyde solution (HCHO, 40 wt%, A.R., Beijing Yili Fine Chemical Reagent Corp.), hydrochloric acid (HCl, A.R.) and acetone (A.R.) were used as received. The water used in all experiments was ultrapure (Millipore, 18.2 MΩ).

Calcined RuO$_2$ powders were used as a referential catalyst in this work. Ruthenium oxide hydrate (RuO$_2$ xH$_2$O, > 45% Ru, Acros) showed no activity towards the cross-dehydrogenative-coupling (CDC) reactions of tetrahydroisoquinolines in our experiment while exhibited activity after calcined in air at 500 ℃ for 5 hours in an oven. XRD revealed that the calcined RuO$_2$ powders were tetragonal phase. The calcined RuO$_2$ powders were grinded before catalytic test and BET adsorption measurement.

1.2 Characterization

TEM:

Samples for transmission electron microscopy (TEM) observation were prepared by drying a drop of ethanol dispersion of the samples on copper grids coated with amorphous carbon membranes. TEM and high-resolution TEM (HRTEM) images were taken on a FEG-TEM (JEM2100F, JEOL, Japan) operated at 200 kV. The average size of the Ru nanoparticles was calculated based on more than 100 particles for each sample.

XRD:

X-ray diffraction (XRD) patterns were obtained on a D/MAX-2000 diffractometer (Rigaku, Japan) with a scanning rate of 1° min^{-1} using Cu Kα radiation. The contributions of Kα$_2$ line in the XRD patterns were subtracted.

XPS:

Imaging Photoelectron Spectrometer (XPS) characterizations were performed on an Axis Ultra (Kratos Analytical Ltd., Japan) imaging photoelectron spectrometer. The ratio of Ru in different oxidation states was determined by fitting the high resolution XPS spectra of Ru-3d electrons in the range of 270 ~ 295 eV. High resolution XPS spectra in Ru-3p region (450 ~ 500 eV) were also collected.

Quantification of Ru nanoparticles:

The concentration of the dispersion of Ru nanoparticles was determined by inductively coupled plasma-atomic emission spectroscopy (ICP-AES). 50 μL of the dispersion was first added in a 25 mL Teflon-lined container and dried. After 4 mL of aqua regia was added, the container was then sealed in a matched steel autoclave and transferred into an oven kept at 180 °C. The autoclave was taken out after 2 hours and cooled to room temperature. The yellow solution was then diluted to 10.0 mL and used for ICP-AES analysis. The ICP-AES analysis was performed on a Profile Spec ICP-AES spectrometer (Leeman, USA).

BET analysts:

Brunauer−Emmett−Teller (BET) specific surface area of the calcined RuO$_2$ powders was measured via nitrogen adsorption at 77 K on an ASAP-2010 analysis system (Micromeritics, U.S.A.).

EPR measurements.
EPR spectra of Figure 6 with the 65 mg solid of Ru nanocatalysts were recorded at 123K on a Bruker ESP-300 spectrometer operating at 9066.397 MHz and a cavity equipped with a Bruker Aquax liquid sample cell. Typical spectrometer parameters were: sweep

time: 2.0 min, center field: 323.090 mT, sweep width 7.5*10 mT, modulation frequency: 100 kHz, modulation width: 1.0*0.1 mT, microwave frequency: 9066.397 MHz; microwave power: 0.99800 mW.

XAFS. Ru K-edge X-ray absorption fine structure (XAFS) analysis was performed by transmission mode on the BL14W1 beamline of Shanghai Synchrotron Radiation Facility (SSRF) operated at 3.5 GeV under "top-up" mode with current of 220 mA.

1.3 TOF determination

Turn over frequency (TOF) of a catalytic process on a certain kind of surface sites is defined as:

$$TOF = N(\text{reagent})/(t \cdot N(\text{site})) = N(\text{reagent})/(t \cdot \sigma(\text{site}) \cdot m(\text{cat.}) \cdot a(\text{cat.}))$$

In this equation, N(reagent) is the total number of the reagent molecule consumed in a certain duration t, and N(site) is the total number of surface sites that are active to the catalytic reaction. σ(site), m(cat.) and a(cat.) are the areal density of active sites on the surface of the catalyst, the mass of catalyst added in the reaction and the specific surface area of the catalyst, respectively. The TOF values were calculated as the conversion of **1a** was lower than 15%.

The outmost Ru atoms on the catalysts were regarded as the sites for the SET process to calculate the apparent TOF values. The areal density of Ru atoms on Ru (0001) facet (the facet with the highest atomic areal density among all facets of hexagonal Ru), 15.8 nm^{-2}, was used as σ(site) of Ru nanoparticles. The areal density of Ru atoms on RuO$_2$ (110) facet (the facet with the highest atomic areal density among all facets of hexagonal RuO$_2$), 10.1 nm^{-2}, was used as σ(site) of RuO$_2$ powders. Using different method to determine the number of sites would result in different apparent TOF value, but would not affect the magnitude of it. The sequence of the TOF values of different catalysts is still reliable.

The specific surface area of Ru nanoparticles was deduced from the morphology and sized distribution of the NPs according to:

$$a(\text{cat.}) = a(P) \cdot w(P) + a(S) \cdot w(S) = (A(P) \cdot V(P) \cdot w(P) + A(S) \cdot V(S) \cdot w(S)) \cdot \rho(\text{Ru})$$

In this equation, a(P), A(P) and V(P) are the specific surface area, surface area and volume of a plate-shaped Ru nanoparticle with the average size and w(P) is the mass fraction of nanoplates in the sample, a(S), A(S), V(S) and w(S) are the corresponding parameters of spherical nanoparticles in the sample. ρ(Ru) is the density of Ru (12.2 g·cm^{-3}). Table S1 shows the size distribution and specific surface area of the Ru nanocatalysts synthesized with different reaction time. Each item listed in the average size in Table S1 was measured based on more than 100 nanoparticles of each morphology.

The specific surface area of RuO$_2$ powders was 11.3 m^2·g^{-1} as measured by BET adsorption technique.

Table S1. The size distributions and specific surface areas of different Ru nanocatalysts.

Sample		Average size (nm)	Surface area (nm²)	Volume (nm³)	Specific surface area (m² g⁻¹)	Mass fraction (%)	Total specific surface area (m² g⁻¹)
Ru-NP-1	plates	$l = 14 \pm 2$ $h = 1.4 \pm 0.2$	313	178	144	70	132
	spheres	$d = 4.6 \pm 0.6$	66	51	106	30	
Ru-NP-2	plates	$l = 15 \pm 3$ $h = 1.4 \pm 0.3$	400	235	139	71	125
	spheres	$d = 5.3 \pm 0.8$	89	79	92	29	
Ru-NP-3	plates	$l = 19 \pm 4$ $h = 1.4 \pm 0.3$	638	389	134	77	123
	spheres	$d = 5.6 \pm 0.9$	99	93	87	23	
Ru-NP-4	plates	$l = 21 \pm 5$ $h = 1.4 \pm 0.4$	759	467	133	78	122
	spheres	$d = 6.0 \pm 0.8$	114	114	82	22	

1.4 Characterizations of Ru nanocatalysts with other morphologies

Ru nanospheres (NSs) separated from Ru-NP-1 and Ru triangular plates (TPs) synthesized with hydrothermal method reported in previous work (Yin, A. X., Liu, W. C., Ke, J., Zhu, W., Gu, J., Zhang, Y.-W., Yan, C.-H. Ru nanocrystals with shape-dependent surface-enhanced Raman spectra and catalytic properties: controlled synthesis and DFT calculations. *J. Am. Chem. Soc.* **134**, 20479-20489 (2012)) were also characterized and used as the catalysts to the SET reaction.

Ru NSs could be separated from the Ru NPs synthesized with the method in this paper through the following procedure: The as-synthesized Ru NPs were first dispersed in 20 mL of mixed solvent of water and acetone (volume ratio 1:1) and filtrated with a syringe filter (pore size 220 nm). Then 20 mL of acetone was added to the filtrate followed by centrifugation at 18,000 rpm for 10 min. The precipitate was washed with water and acetone (volume ratio 1:5) for three times and then dispersed in methanol.

Ru TPs were synthesized with the following procedure: 100 mg of PVP was first dissolved in 10 mL of water, followed by adding 0.06 mmol RuCl₃ xH₂O and 0.4 mL of formaldehyde solution (40 wt%). The solution was then diluted to 15 mL, loaded in a 25 mL Teflon-lined container and sealed in a matched steel autoclave. The autoclave was then heated in an oven kept at 160 ℃ for 4 h. After the reaction, 45 mL acetone was added and the product was then collected by centrifugation at 7,800 rpm for 10 min.

Figure S5 shows the TEM images and XPS spectra of Ru NSs and Ru TPs. These two kinds of Ru NPs were also used to catalyse the CDC reaction in Table S6. The TOF values and the surface oxidation levels ($Ru^{n+}/(Ru^{0}+Ru^{n+})$) agreed well with the volcano-shaped relationship, as discussed in Figure S5c.
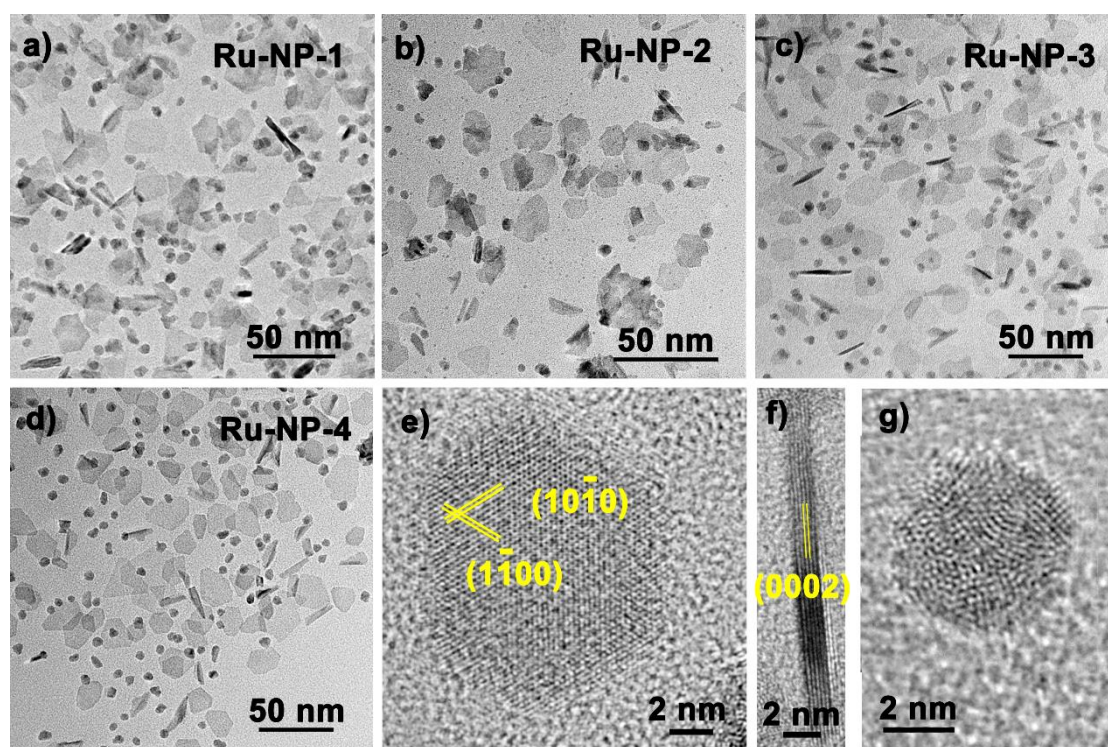
1.5 Supplementary figures and tables

Figure S1. TEM images of (a) Ru-NP-1, (b) Ru-NP-2, (c) Ru-NP-3 and (d) Ru-NP-4, and HRTEM images of representative plate-shaped Ru NPs in Ru-NP-1 from (f) top-view and (g) side-view, and a spherical Ru nanoparticle. The lattice fringes corresponding to *hcp* Ru are marked in panel (e) and (f). The Ru nanosphere in panel (g) is a poly-crystalline particle with very small domain.
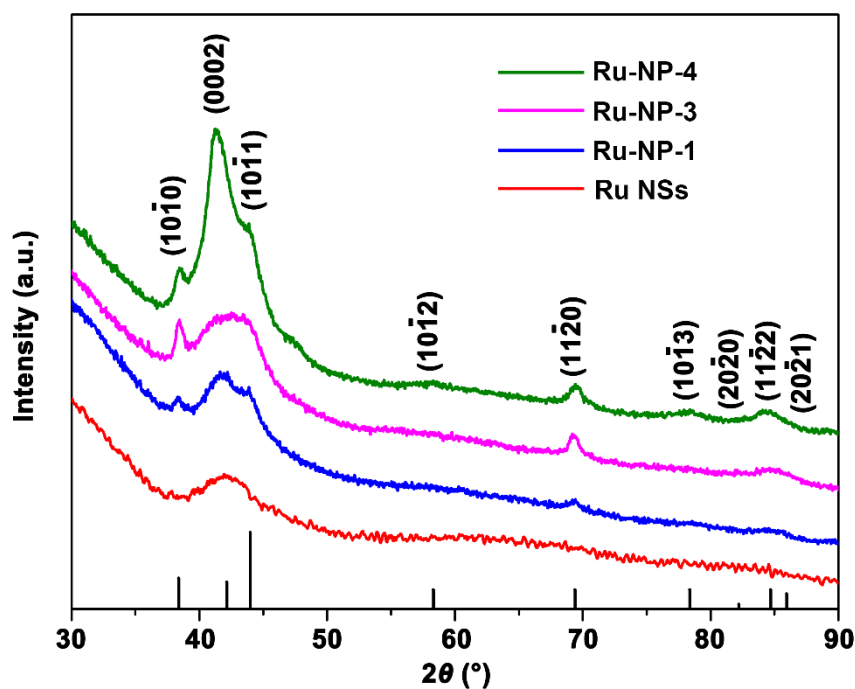
Figure S2. XRD patterns of Ru-NP-1 (blue line), Ru-NP-3 (pink line), Ru-NP-4 (green line) and Ru NSs separated from Ru-NP-1 (red line). The black vertical lines are the standard diffraction peaks of hexagonal closest packed (*hcp*) Ru (JCPDS card no. 06-0663). Because of the weak crystallinity of Ru NSs, the diffraction peaks broaden seriously. The intensities of the diffraction peaks of Ru-NP-4 are significantly higher than that of other samples, indicating that the sample crystallinity increased substantially as the reaction time was extended from 16 h to 24 h. Because the thicknesses of the NPs in *c* direction are around 1.4 nm, the diffraction peaks with the index of (*hkl*) ($l \neq 0$) broaden obviously.
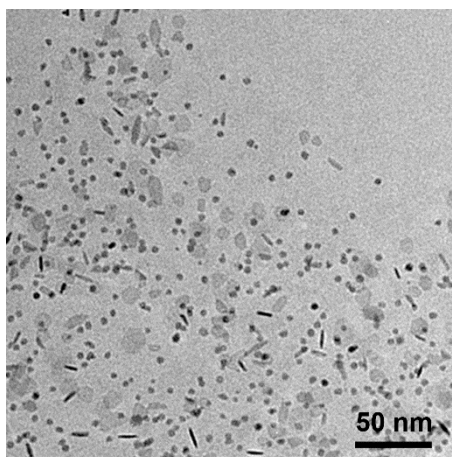
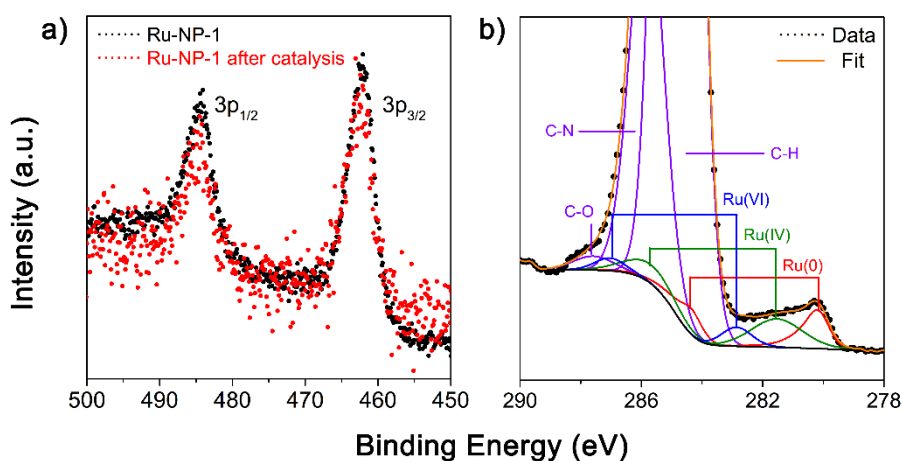**Figure S3.** TEM image of Ru-NP-1 after the catalytic reaction.

Figure S4. (a) XPS spectra of Ru-NP-1 before (black dots) and after (red dots) catalysis test in Ru-3p region. (b) XPS spectrum of Ru-NP-1 after catalysis test in Ru-3d and C-1s region. The fitting results of Ru-3d spectra are shown in Table 3, which are similar to that of the as-synthesized sample. Due to the adsorption of the product molecules on the surface of Ru nanoparticles, the XPS signals of Ru after the catalysis test were weaker than that of the as-synthesized sample. Whereas, both the spectra in Ru-3d and Ru-3p regions show that the oxidation level of Ru-NP-1 did not obviously change after the catalytic test. The blue and green vertical lines indicate the binding energy of Ru(0) and Ru(IV) states, respectively.
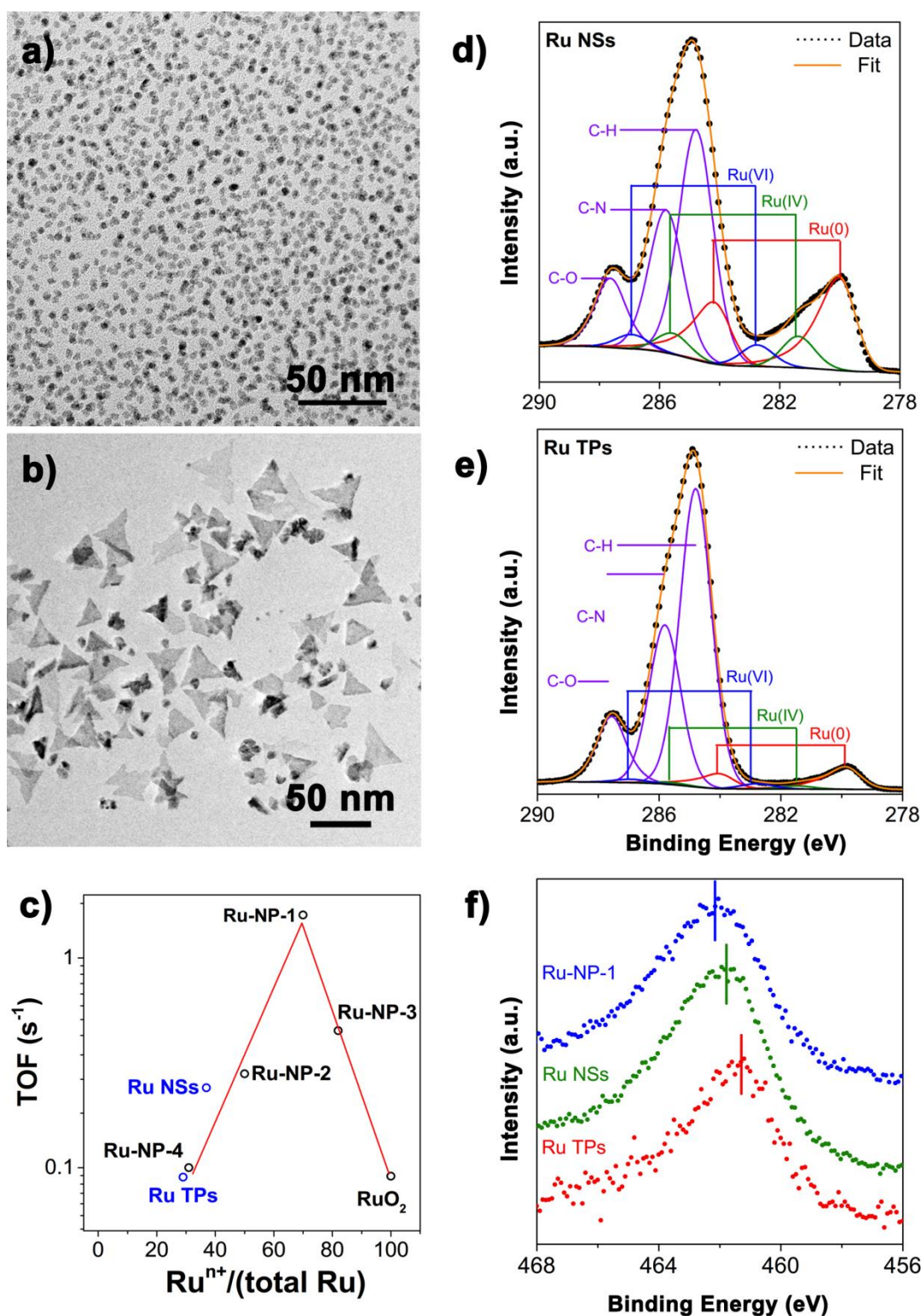
Figure S5. TEM images of (a) Ru NSs separated from Ru-NP-1 and (b) hydrothermally synthesized Ru TPs, and (c) the corresponding plots of TOF values of Ru NSs and TPs catalysing the CDC reactions in Table S6 against their surface oxidation level quantified as the percentage of surface Ru atoms in positive valences among all surface Ru atoms deduced from Ru-3d XPS spectra. The plots agreed well with the volcano-shaped relation in Figure 7. Ru NSs separated from Ru-NP-1 showed significantly lower activity than Ru-NP-1, indicating that the excellent catalytic activity of Ru-NP-1 mainly derive from the plate-shaped Ru NPs. (d, e) Ru-3d XPS spectra. (f) XPS spectra of Ru 3p electrons of Ru-NP-1, NSs and TPs. Binding energy for Ru metallic and oxide levels were marked by vertical lines.
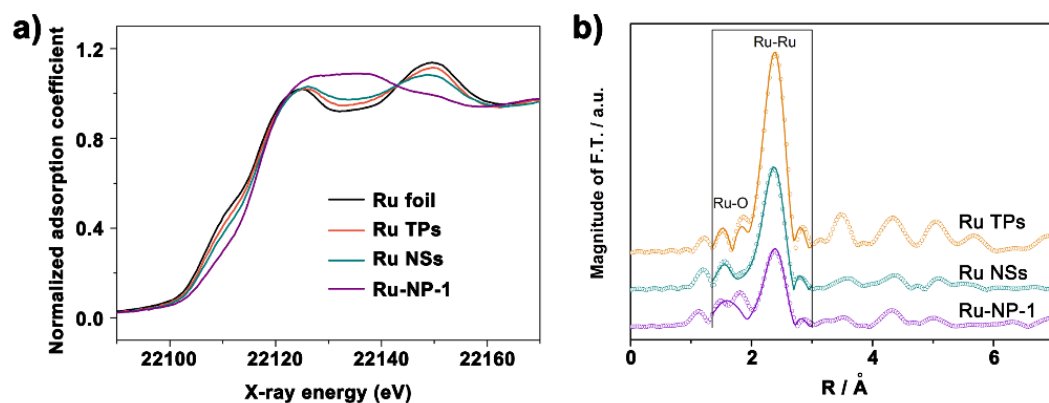
Figure S6. (a) XANES spectra and (b) *r*-space EXAFS spectra and the curve fitting for Ru K-edge of Ru-NP-1, NSs and TPs. Ru foil was used as a reference.

Table S2. Data fitting of Ru K-edge EXAFS and Ru 3p XPS spectra of Ru HPs, NSs and TPs: coordination number and interatomic distance in Ru-O and Ru-Ru shells (EXAFS), binding energy and ratio of Ru in metallic and oxide states (XPS).

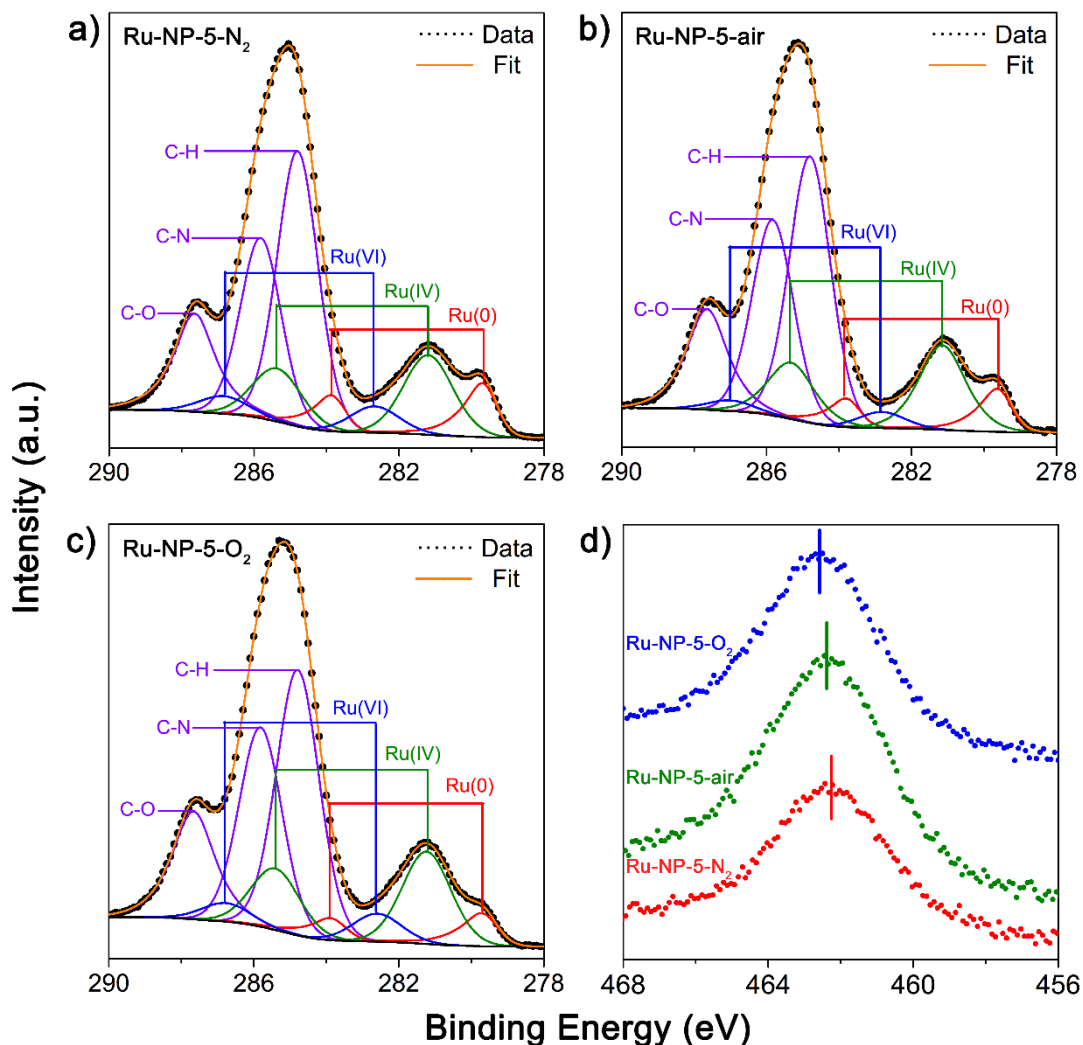| Sample | EXAFS | | | | XPS | | |
| | Ru-O shell | | Ru-Ru shell | | Ru 3p BE / eV | | $Ru^0:Ru^{n+}$ |
	R / Å	CN	R / Å	CN	Ru^0	Ru^{n+}	
Ru-NP-1	2.03±0.02	2.4±0.9	2.69±0.01	3.9±0.9	461.4	462.7	30:70
Ru NSs	1.98±0.02	1.0±0.4	2.673±0.005	7.0±0.7	461.2	462.8	63:37
Ru TPs	1.94±0.05	0.6±0.6	2.683±0.005	8.5±0.8	461.2	462.9	71:29

Figure S7. XPS spectra of Ru nanoparticles prepared under different atmospheres, such as Ru-NP-5-N_2, Ru-NP-5-air, Ru-NP-5-O_2. (a–c) The spectra are presented and fitted in C-1s and Ru-3d region. Each spectrum was deconvolved into C-1s peaks at 284.8 eV, 285.8 eV and 287.6 eV (violet curves), which were assigned to C atoms in C-H, C-N and C=O forms, respectively. These spectra were also deconvolved into Ru-3d doublets (3d$_{5/2}$ and 3d$_{3/2}$, Δ = 4.17 eV) with the binding energy of Ru 3d$_{5/2}$ peak at 279.5 – 279.9 eV, 281.2 – 281.4 eV and 282.6 – 282.8 eV, which were assigned to Ru(0) (red curves), Ru(IV) (green curves) and Ru(VI) (blue curves) states respectively. The fitting results of Ru-3d spectra are shown in Table 3. (d) The spectra are presented and fitted in Ru-3p$_{3/2}$ region. The red, green and blue lines represent the binding energy of Ru(0), Ru(IV) and Ru(VI) states, respectively.

Table S3. XPS data fitting results of all the catalysts in Ru-3d region.

Sample	Ru(0)		Ru(IV)		Ru(VI)	
	B. E. / eV [a]	Ratio / %	B. E. / eV	Ratio / %	B. E. / eV	Ratio / %
Ru-NP-5-N_2	279.7	23	281.2	58	282.7	19
Ru-NP-5-air	279.6	20	281.1	68	282.8	12
Ru-NP-5-O_2	279.7	15	281.2	65	282.6	20

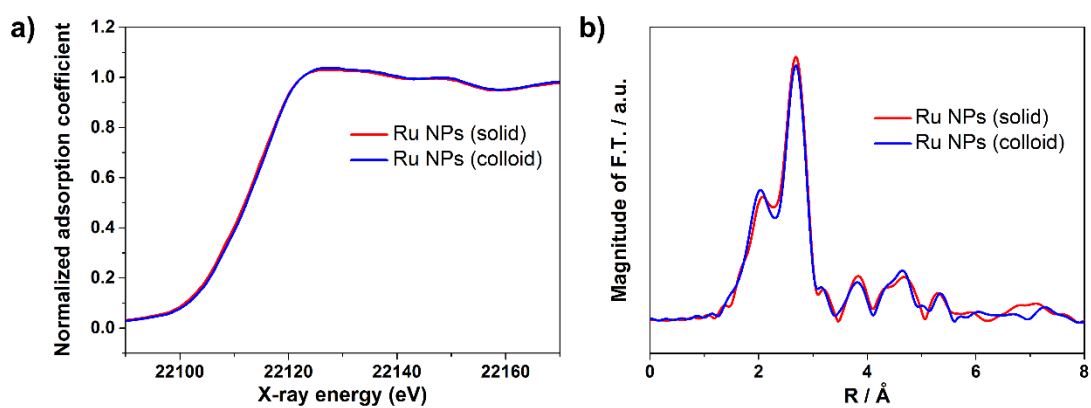[a] B. E., binding energy of Ru 3d$_{5/2}$ electrons.

Figure S8. (a) XANES spectra and (b) *r*-space EXAFS spectra and the curve fitting for Ru K-edge of Ru NPs tested as solid powders and colloid in MeOH.
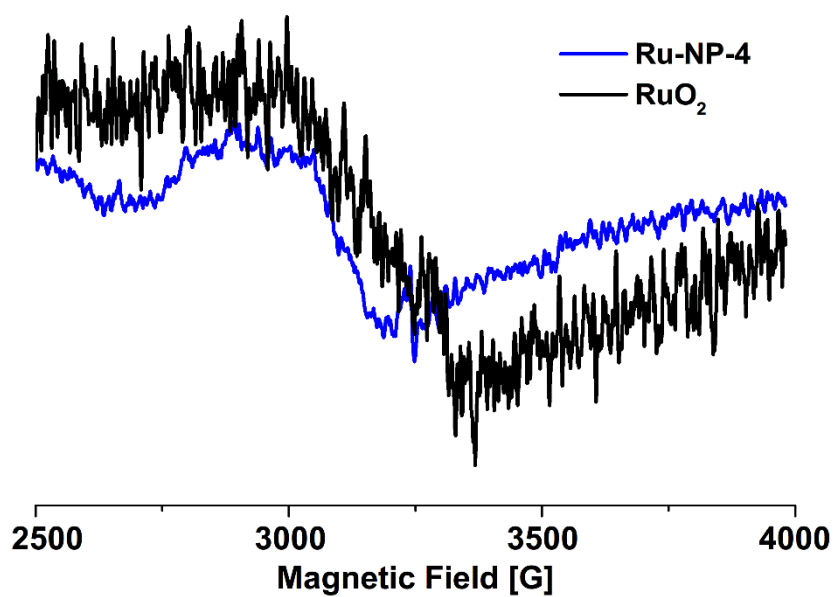

Figure S9. EPR spectra of Ru-NP-4 (blued curve) as solid powders and RuO_2 powders (black curve) collected at 123 K (microwave frequency 9066.397 MHz; microwave power 0.99800 mW).
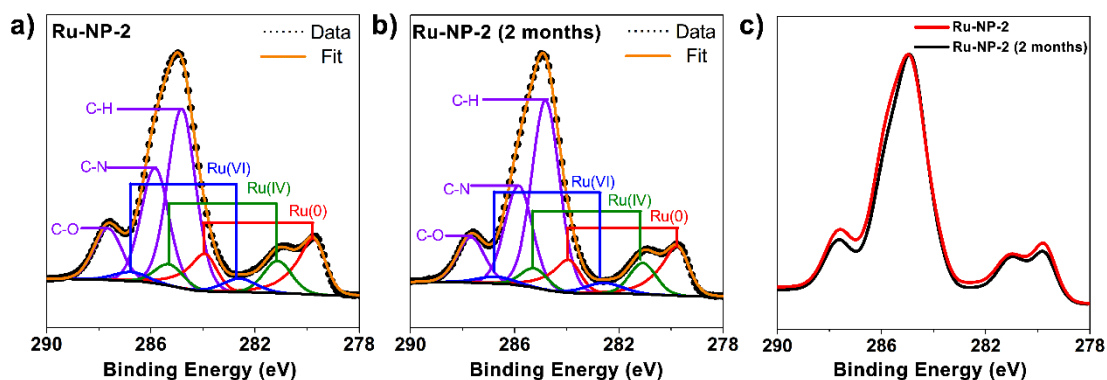
Figure S10. XPS spectra of Ru-NP-2 tested as newly synthesized and 2 months later. (a-b) The spectra in C-1s and Ru-3d region. Each spectrum was deconvolution into C-1s peaks at 284.8 eV, 285.8 eV and 287.6 eV (violet curves), assigned to C atoms in C-H, C-N and C=O forms respectively, and Ru-3d doublets (3d5/2 and 3d3/2, Δ = 4.17 eV) with the binding energy of Ru 3d5/2 peak at 279.5 ~ 279.9 eV, 281.2 ~ 281.4 eV and 282.6 ~ 282.8 eV were assigned to Ru(0) (red curves), Ru(IV) (green curves) and Ru(VI) (blue curves) states respectively. (c) The spectra in Ru-3p3/2 region.

Table S4. XPS data fitting results of all the catalysts as newly synthesized and 2 months later in Ru-3d region.

Sample as newly-syntheized	Ru(0)		Ru(IV)		Ru(VI)	
	B. E. / eV ^{a}	Ratio / %	B. E. / eV	Ratio / %	B. E. / eV	Ratio / %
Ru-NP-1	279.8	30	281.2	50	282.7	20
Ru-NP-2	279.7	50	281.1	33	282.7	17
Ru-NP-3	279.7	18	281.2	63	282.7	18
Ru-NP-4	279.5	69	281.1	31	--	0

Sample as syntheized 2 months later	Ru(0)		Ru(IV)		Ru(VI)	
	B. E. / eV	Ratio / %	B. E. / eV	Ratio / %	B. E. / eV	Ratio / %
Ru-NP-1	279.9	30	281.3	52	282.6	18
Ru-NP-2	279.8	51	281.1	33	282.6	16
Ru-NP-3	279.9	19	281.3	61	282.5	19
Ru-NP-4	279.4	67	281	33	--	0

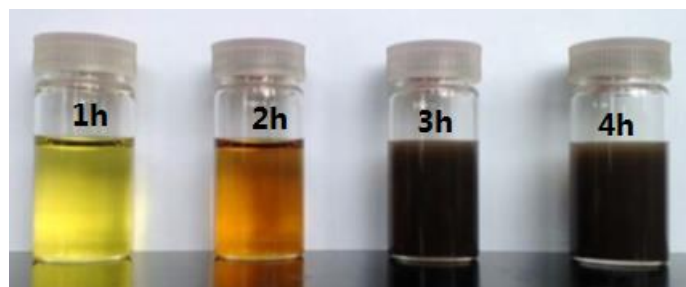^{a} B. E., binding energy of Ru $3d_{5/2}$ electrons.

Figure S11. Digital images of the reaction solution for the synthesis of Ru nanocrystals after hydrothermal treatment at 160 ℃ for different reaction times (1-4 h). The "0 h" sample was the mixture of reagents initially added. Greenish yellow solutions were formed during the first 2 hours of the synthesis, and deep grey to black dispersions were obtained after 3 h of reaction. In the synthesis (RuCl$_3$•xH$_2$O as precursor with sodium oxalate (Na$_2$C$_2$O$_4$)), Ru(III) species were in the form of [Ru(III)(ox)$_3$]$^{3-}$ (ox = oxalate) before being reduced by HCHO, as confirmed by the color of the reaction solutions. Ru(III) oxalates [Ru(III)(ox)$_3$]$^{3-}$) were generated in the first hour of the hydrothermal treatment.

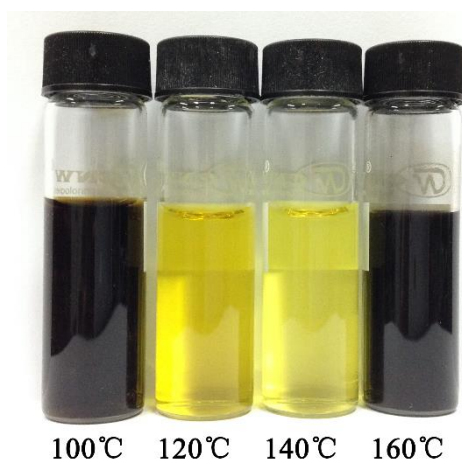
100℃   120℃   140℃   160℃

Figure S12. Digital images of the reaction solution for the synthesis of Ru nanocrystals after hydrothermal treatment at 8 h for different reaction temperatures (100 ℃ -160 ℃). HCHO as the reductant did not work below/including 140 ℃, as confirmed the extinction spectra and the color of the reaction solutions.
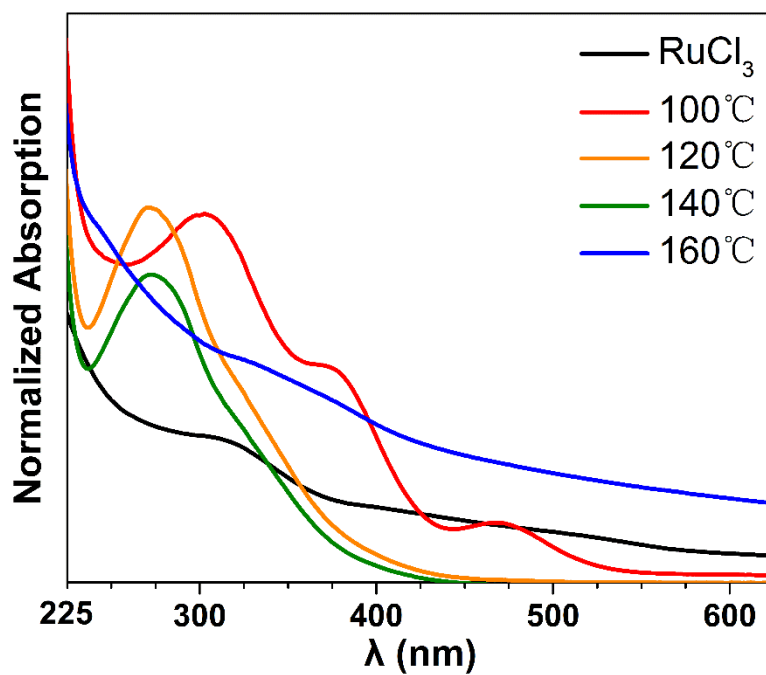
Figure S13. Temperature-sequential extinction spectra of the solutions or dispersions obtained from the synthetic reaction of Ru NPs.

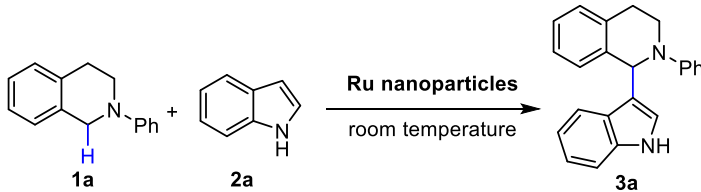## 2. Ru-Nanocatalyzed Cross-Dehydrogenative-Coupling Reactions

2.1 General

Reactions were stirred using Teflon-coated magnetic stir bars. Elevated temperatures were maintained using Thermostat-controlled silicone oil baths. Organic solutions were concentrated using a Büchi rotary evaporator with a desktop vacuum pump. Synthetic reagents were purchased from Acros, Aldrich, Alfa Aesar, Beijing Chemical Works, Beijing Yili Fine Chemical Reagent Corp. and used without further purification, unless otherwise indicated. Analytical TLC was performed with 0.25 mm silica gel G plates with a 254 nm fluorescent indicator. The TLC plates were visualized by ultraviolet light and treatment with phosphomolybdic acid stain followed by gentle heating. Purification of products was accomplished by flash chromatography on silica gel and the purified compounds showed a single spot by analytical TLC.

NMR spectra were measured on Bruker ARX 400 (^{1}H at 400 MHz, ^{13}C at 100 MHz), Bruker ARX 500 (^{1}H at 500 MHz, ^{13}C at 126 MHz) nuclear magnetic resonance spectrometers. Data for ^{1}H-NMR spectra are reported as follows: chemical shift (ppm, referenced to TMS; s = singlet, d = doublet, t = triplet, q = quartet, dd = doublet of doublets, dt = doublet of triplets, dm = doublet of multiplet, ddd = doublet of doublet of doublets, tdd = triplet of doublet of doublets, m = multiplet), coupling constant (Hz), and integration. Data for ^{13}C-NMR are reported in terms of chemical shift (ppm) relative to residual solvent peak (Acetone [$(CD_3)_2CO$]: 2.05 ppm). Infrared spectra were recorded on Mettler-Toledo ReactIR iC10 system with an SiComp probe and are reported in wavenumbers (cm^{-1}). High-resolution mass spectra (HRMS) were recorded on a Bruker Apex IV FTMS mass spectrometer (ESI). Optical rotations were measured on a Perkin-Elmer 341 LC spectrometer.
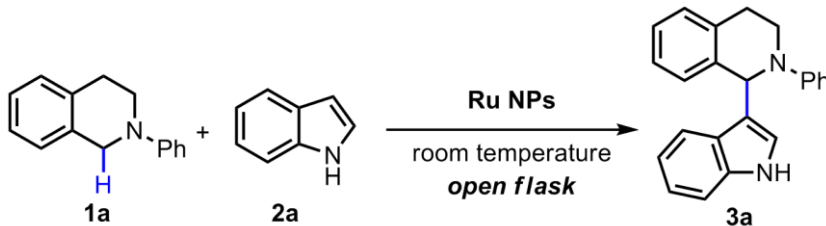
2.2 Optimization of standard conditions

Our test of the novel Ru nanoparticles-catalyzed CDC reactions started with the optimization studies. *N*-phenyl-1,2,3,4-tetrahydroisoquinoline **1a** and indole **2a** were employed as the model substrates to study the influence of catalyst, additive and solvent on the reaction (Table S5). Two substrates were directly put into Ru-NP-1's dispersing water phase. Unfortunately, no reaction occurred with poor solubility of substrates **1a** and **2a** in water (entry 1). Thus, methanol as co-solvent with water was preferred and the reaction system gave expected C-H functionalized product **3a** (entry 2). However, byproduct **6** was accompanied, which represents that the deprotonation pathway occurred showed in the mechanism of Figure S6. Thus, AcOH was added in order to avoid the deprotonation of the aminium radical cation towards byproduct **6**,[S1] via increasing the concentration of hydrogen ions in the reactive system.[S2] As expected, the C(sp^3)-H functionalized product **3a** was achieved in the yield of 94% (entry 3). We then studied how solvent affected the reactions, finding that higher yield can be obtained in H_2O/CH_3OH than others (entries 3-6). If the Ru nanocatalyst was removed from the reactive system, no reaction occurred only with AcOH (entry 7). Of course, if the reaction of tetrahydroisoquinoline 1a and nitromethane catalyzed by Ru nanocatalysts was conducted in 60 ℃, the reaction time could be greatly reduced to only 2 hours with the yield of 93%.

Table S5. Optimization studies on the Ru nanoparticles-catalyzed CDC reactions[a]

entry	catalyst[b]	additive	solvent[c]	time[h]	yield[%][d]
1	Ru-NP-1	_	H_2O	72	no reaction
2	Ru-NP-1	_	H_2O/CH_3OH	96	42[e]
3	Ru-NP-1	AcOH	H_2O/CH_3OH	42	94
4	Ru-NP-1	AcOH	H_2O/CH_3CN	72	trace
5	Ru-NP-1	AcOH	H_2O/DMF	72	trace
6	Ru-NP-1	AcOH	$H_2O/EtOH$	50	87
7	_	AcOH	H_2O/CH_3OH	72	no reaction

[a] Reaction conditions: 8 mol % of Ru nanocatalyst (measured in accordance with Ru element mass), 1 equiv. of **1a**, 4 equiv. of **2a**, 48 μL AcOH, 0.025 M in concentration. [b] Ru nanoparticles with preparation for 8 hours. [c] H_2O/CH_3OH 1:1, H_2O/CH_3CN 1:1, H_2O/DMF 1:1. [d] Isolated yield after column chromatography. [e] 29% of **6** as the byproduct was accompanied.

Table S6. Catalytic properties on CDC reactions with different Ru catalysts[a]

entry	catalyst	equiv.[b]	Time [h]	Conversion [%]	Yield [%][c]	TOF [s^{-1}][d]
1	Ru-NP-1	8 mol %	42	100	94	1.6
2	Ru NSs	8 mol %	48	82	43	0.24
3	Ru TPs	8 mol %	72	5	Trace	0.012
4	RuO_2	80 mol %	45	30	18	0.091
5	$RuCl_3 \cdot xH_2O$	8 mol %	72	0	no reaction	_

[a] Reaction conditions: 0.10 mmol of **1a**, 4 equiv. of **2a**, 16 equiv. of AcOH, 0.025 M in concentration, solvent: H_2O/CH_3OH 1:1, room temperature. [b] Molar ratio of Ru element to reagent **1a**. Inductively coupled plasma-atomic emission spectroscopy (ICP-AES) was used for the quantification of Ru element. [c] Isolated yield after column chromatography. [d] The TOF was obtained with the conversion of **1a** lower than 15%. The number of sites was calculated from the specific surface area of the sample and the density of the outmost Ru atoms on the surface. For Ru NPs, the specific surface area was deduced from the morphology and average size of the NPs, and the atomic density of Ru (0001) facet was approximately used as the site density on the surface. For RuO_2, the specific surface area was measured by BET adsorption and the density of Ru atoms on RuO_2 (110) facet was approximately used as the site density on the surface. Using different method to determine the number of sites would result in different apparent TOF value, but would not affect the magnitude of it.
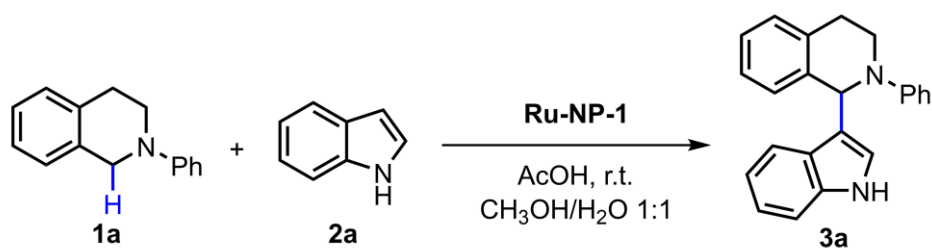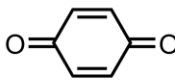
2.3 Mechanism

We now have systematically clarified the mechanism as showed in Figure S8. In the SET process, Ru nanoparticles captured one single electron from tetrahydroisoquinoline derivative **1a** with lone pair electrons to generate aminium radical cation **A** and transferred it to oxygen from air to form the superoxide anion radical ($O_2^{\cdot -}$), which is the impetus of this reaction. Then iminium ion **B** could be achieved by several conversions following the formation of radical intermediate **A** and be attacked by nucleophiles yielding the final complex molecules. Three possible pathways towards the desired iminium ion **B** were proposed.[S3,S4] In the pathway a, 1,2-hydrogen shift may happen and furnish the carbon centered radical **C**, which can now be easily deprotonated by a base and yield the iminium ion **B**. In the pathway b, the deprotonation may initially take place and provide carbon centered neutral radical **D**, undergoing electron transfer to afford the the iminium ion **B**. However, the reaction system is acidic owing to AcOH, so that the deprotonation is completely difficult. And the control experiments also showed that when there was no AcOH, the byproduct lactam compound **6** could be afforded by oxidation of carbon centered neutral radical **D/E** in the pathway b, while no byproduct **6** was observed by addition of AcOH in the reaction system (entry 2 in Table S2). The presence of final product even without proton acid in the reaction system suggests that formation of the iminium ion **B** may not proceed *via* both the deprotonated pathways a and b, but the byproduct **6** here alludes that protons have effects in inhibiting side reactions. The most plausible mechanism is pathway c, that hydrogen atom ($H^{\cdot}$) abstraction takes place from the aminium radical cation **A** to achieve the desired iminium ion **B**.

This mechanism can be generally divided into these steps: the ionization of amine generating the aminium radical cation, then ensuing hydrogen atom abstraction forming the iminium cation intermediate, finally the nucleophilic addition to iminium cation leading to the final product, and we can now construe our experimental observations with it. The Ru nanoparticles with moderate oxidation level contribute mainly to the first step by facilitating the ionization. The substitutes on the *N*-aryl (**3a**, **3k**, **3l** and **3m** in Table 4 have dual effects on reactivity of substrates: in ionization, the electron-withdrawing group (**3m**) improves the potential to remove an electron from amine generating the aminium radical cation, hence impedes the ionization and cause the incomplete conversion of substrate, electron-donating groups (**3k**) facilitates the ionization thus complete conversion is observed with relatively short time consumed. In the nucleophilic addition, on the other hand, the electron-donating group stabilizes the intermediate iminium cation and meanwhile provides the superoxide radical anion generated in situ enough time to react with iminium cation before its depleted resulting the byproduct amide. This explication makes the relative low yield from product **3k** with fast consumption comprehensible, and also construes the slow consumption but relative high yield from product **3m** attributes to the high reactivity of iminium cation generated by product **3m** with drastic electron-withdrawing effects of *meta*-fluoro substitute.

$O_2^{\cdot -}$ radical comes to water finally. The reaction was carried out in CD_3OD without AcOH, which also could achieved the final product (entry 2 in Table S5), and the amount of H_2O (and HDO) formation was determined by ^{1}H NMR. Two moles of HDO were regarded as one mole of H_2O. This has been verified experimentally and theoretically in previous studies, such as: *J. Phys. Chem. A* **2005**, *109*, 6089; *J. Am. Chem. Soc.* **2012**, *134*, 4625; *J. Am. Chem. Soc.* **2005**, *127*, 6632; *J. Phys. Chem. A* **2005**, *109*, 6089.

Table S7. Mechanism study of Ru-nanocatalyzed cross-dehydrogenative-coupling reactions.[a]

entry	atmosphere	additive	time[h]	yield[%][b]
1	N_2	–	42	no reaction
2	O_2	–	16	94
3	air	–	42	94
4	air	(quinone)	72	no reaction

[a] Reaction conditions: 0.10 mmol of **1a**, 4 equiv. of **2a**, 48 μL AcOH, 0.025 M in concentration, solvent: H_2O/CH_3OH 1:1, room temperature. [b] Isolated yield after column chromatography.
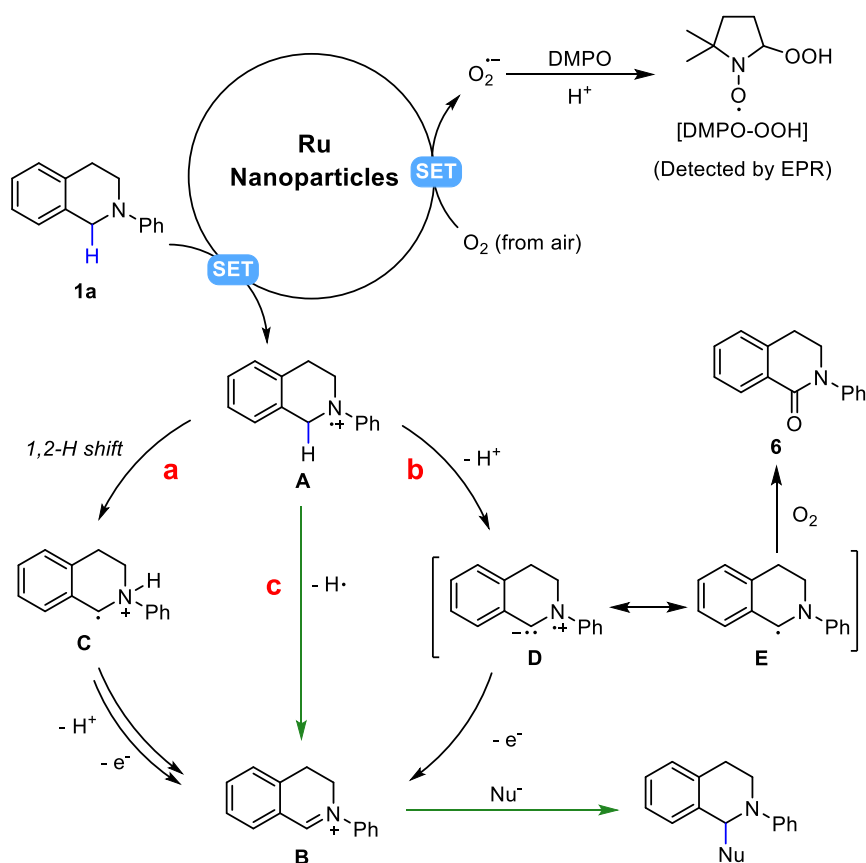

Figure S14. Ru-nanocatalyzed SET mechanism.

2.4 Catalytic activity comparison

Compared with homogeneous CDC reactions, the strategy of heterogeneous catalysis is desirable due to its numerous advantages, namely catalyst recyclability, continuous flow processes and ease of catalyst removal from the reaction mixture, that homogeneous catalysis can not realize. With the development of green chemistry, the difficulty of catalyst separation from the final

product in homogeneous systems creates economic and environmental barriers to broadening their scope. Meanwhile, most of those CDC reactions require necessary tough oxidants or reductants, light energy supplement, and/or high temperature. In 2010, Stephenson and his co-workers reported the first application of transition metal photocatalysts to cross-dehydrogenative-coupling (CDC) reactions of amines *via* a SET process (Figure S15a).

Nanocatalysis has been studied as a new frontier in heterogeneous catalysis, that bridges homogeneous and heterogeneous catalytic processes. Insolubility of nanoparticles (NPs) as catalyst in the reaction solvents makes ease of separation from the reaction system like heterogeneous catalysts. Furthermore, composition- and structure-controlled NPs present different catalytic behaviors owing to the modulation of their electronic and geometric structures.[S9] Due to high activity of Ru photocatalysts in the CDC reactions, we were eager to introduce Ru NPs containing Ru cations on their oxidative surface instead of homogeneous Ru(III) catalysts, to explore their catalytic possibilities for a predictable, highly selective, and efficient methodology under ambient conditions, which is a long-expected goal for all the homogeneous, heterogeneous and enzymatic catalysis (Figure S15b).[S8, S10]
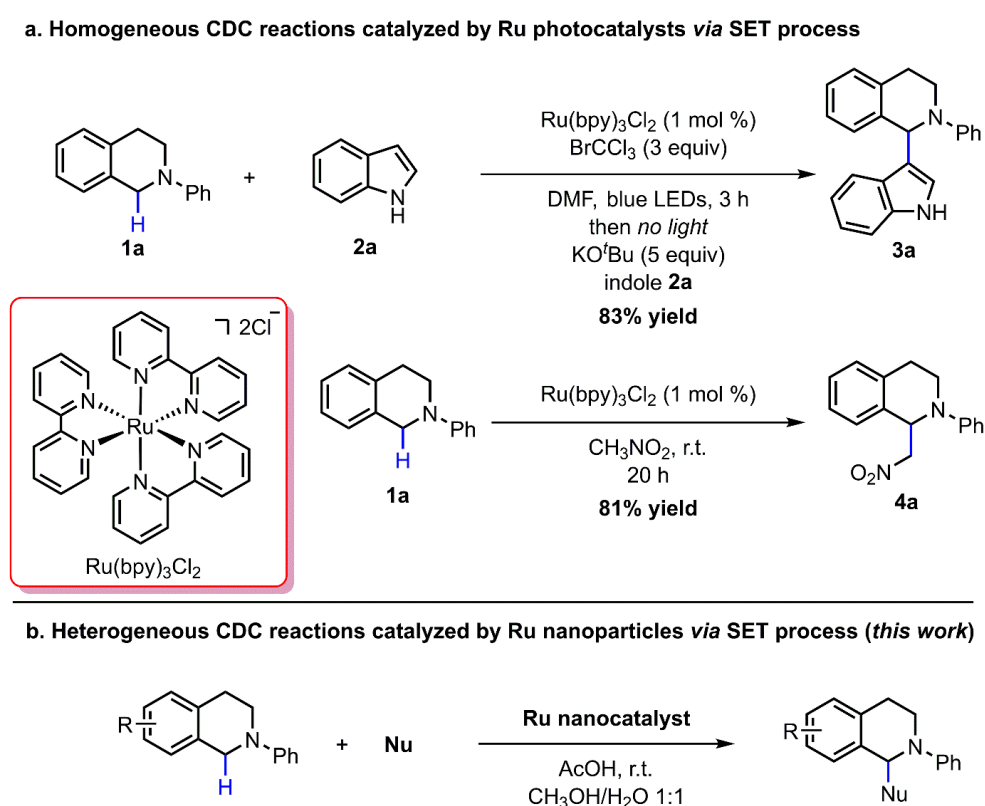
a. Homogeneous CDC reactions catalyzed by Ru photocatalysts *via* SET process

b. Heterogeneous CDC reactions catalyzed by Ru nanoparticles *via* SET process (*this work*)

Figure S15. Homogeneous and Heterogeneous Ru-catalyzed CDC reactions.

2.5   Hammett study

General procedure: The concentration of Ru NPs colloidal methanol solution was determined by ICP-AES. 72 μL methanol solution of Ru-NP-1 (5.61 mg/mL, 8 mol %), 0.05 mmol *meta* or *para*-substituted tetrahydroisoquinoline, 0.5 mL CH_3NO_2, 48 μL AcOH were added into a reaction tube. The mixture was stirred at 40 °C. Control the conversion ratio of tetrahydroisoquinoline substrate under 15%. Then, 0.05 mmol benzophenone was added into the system as an internal standard and the mixture was extracted with ethyl ether. The organic layer was test by GC to confirm the conversion ratio of tetrahydroisoquinoline substrate.

Table S8. Results of Hammett study

entry	substrate	reaction time [h]	conversion ratio [%]	log(v)	σ

1	*p*-OMe	0.1	10.5	0.0204	-0.27
2	*p*-Me	0.1	3.8	-0.4200	-0.17
3	H	0.5	8.0	-0.7959	0
4	*p*-Br	2.8	12.5	-1.3510	0.39
5	*p*-CF$_3$	3.0	5.0	-1.7813	0.54
6	*m*-NO$_2$	6.5	7.4	-1.9459	0.71

2.6 EPR study

EPR measurements.[S5] EPR spectra of Figure 3 were recorded at room temperature on a Bruker ESP-300 spectrometer operating at 9.7 GHz and a cavity equipped with a Bruker Aquax liquid sample cell. Typical spectrometer parameters were: Typical spectrometer parameters were: sweep time: 4.0 min, center field: 323.100 mT, sweep width 5*1 mT, modulation frequency: 100 kHz, modulation width: 1.0*0.1 mT, microwave frequency: 9056.103 MHz; microwave power: 4.0 mW. DMPO (5-,5-dimethyl-1-pyrroline *N*-oxide) was employed as the radical trap.

Control experiments (Table 1 in the manuscript) suggest that oxygen in this reaction may capture single electron to generate active radical species (O$_2^{\cdot-}$) in the acidic system, which could undergo radical coupling with another molecule of DMPO radical to form [DMPO-OOH]. As expected, the formation of the [DMPO-OOH] intermediate was identified by monitoring the Ru-nanocatalyzed SET process of oxygen with DMPO by EPR spectroscopy. EPR spectra were recorded from the standard reactive system of CDC reactions. No obvious signal was present without Ru nanocatalyst, AcOH, or oxygen separately.

2.7 Experimental details

General procedure: The concentration of Ru nanoparticles colloidal methanol solution was determined by ICP-AES. Ru-NP-1 (5.61 mg/mL, 8 mol %) was calculated in accordance with Ru element mass and added into the solvents (H$_2$O/CH$_3$OH 1:1) with 1 equiv. of tetrahydroisoquinoline derivatives, 4 equiv. of indoles and 10-48 μL AcOH. The mixture (0.025 M in concentration) was stirred under room temperature. The reaction tube was immersed under room temperature. When TLC indicated the disappearance of the starting material, the reaction mixture was filtered through a thin pad of silica gel. The filter cake was washed with PE/EA, and the combined filtrate was concentrated. The crude product was purified by flash column chromatography on silica gel to afford the corresponding final product.
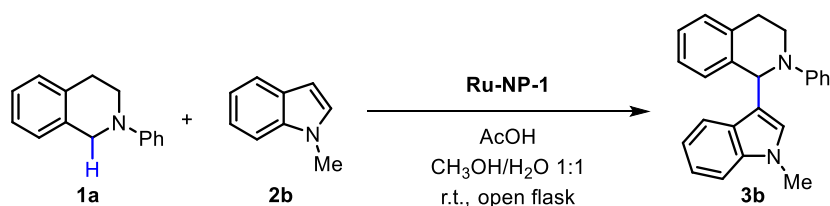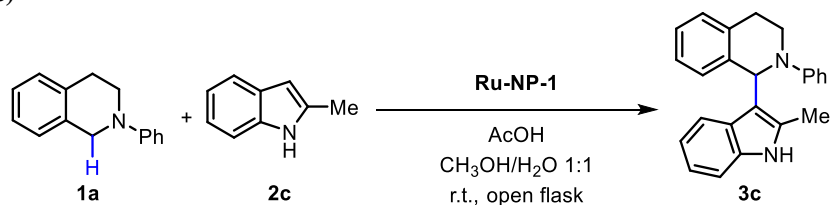
Experimental Data

Product (3a)
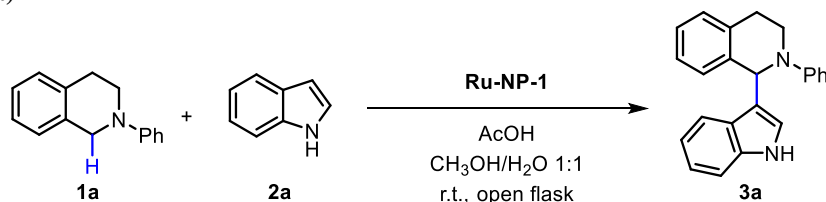
Reaction time: 42 h. Following the general procedure, tetrahydroisoquinoline **1a** (10.3 mg, 0.05 mmol) and indole **2a** (23.4 mg, 0.20 mmol) was converted to product **3a**[S6] (15.0 mg, 0.046 mmol) in 94% yield. On gram scale, tetrahydroisoquinoline **1a** (1.00 g, 4.78 mmol) and indole **2a** (2.24 g, 19.12 mmol) was converted to product **3a** in 91% yield determined by NMR using 4-nitroacetophenone as an internal standard.
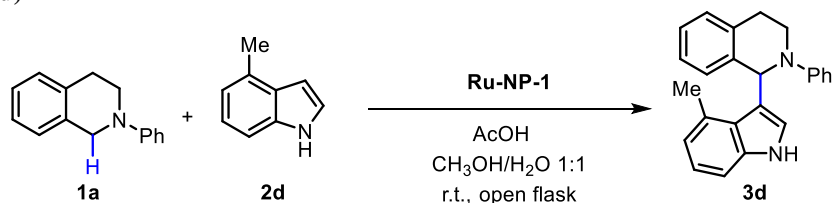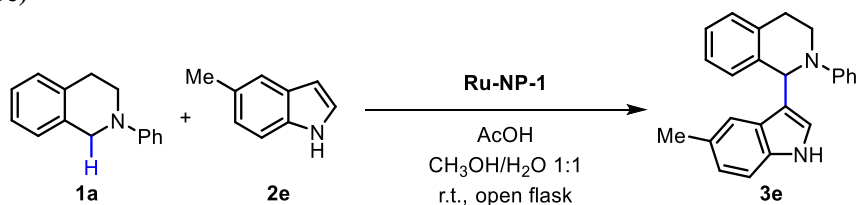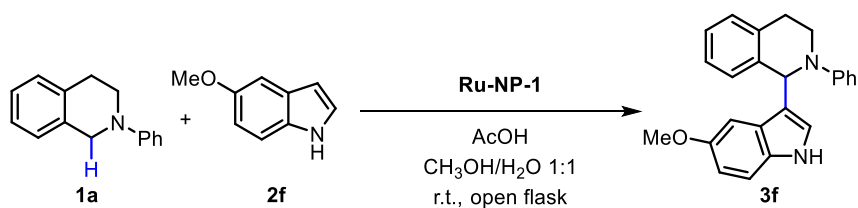
Product (3b)

1a + **2b** → **3b**

Reaction time: 57 h. Following the general procedure, tetrahydroisoquinoline **1a** (20.6 mg, 0.10 mmol) and indole **2b** (52.4 mg, 0.40 mmol) was converted to product **3b**[S6] (31.9 mg, 0.094 mmol) in 96% yield.
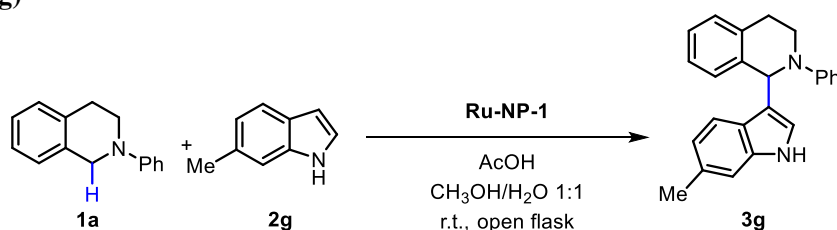
Product (3c)

1a + **2c** → **3c**

Reaction time: 57 h. Following the general procedure, tetrahydroisoquinoline **1a** (21.4 mg, 0.10 mmol) and indole **2c** (52.4 mg, 0.40 mmol) was converted to product **3c**[S6] (10.0 mg, 0.030 mmol) in 29% yield.

Product (3d)

1a + **2d** → **3d**

Reaction time: 51 h. Following the general procedure, tetrahydroisoquinoline **1a** (21.8 mg, 0.10 mmol) and indole **2d** (52.4 mg, 0.40 mmol) was converted to product **3d** (13.4 mg, 0.040 mmol) in 38% yield.

3d: White solid: TLC R_f (10% EA/PE) = 0.14, mp = 220-222 °C. ^{1}H NMR (500 MHz, Acetone): δ 9.99 (s, 1H), 7.35 – 7.31 (m, 1H), 7.21 (d, J = 8.1 Hz, 1H), 7.20 – 7.08 (m, 7H), 7.04 – 6.92 (m, 1H), 6.80 – 6.68 (m, 2H), 6.37 (s, 1H), 6.34 (d, J = 2.5 Hz, 1H), 3.78 – 3.67 (m, 2H), 2.92 – 2.83 (m, 1H), 2.63 – 2.53 (m, 4H). ^{13}C NMR (126 MHz, Acetone): δ 150.9, 138.8, 138.6, 136.5, 131.9, 129.83, 129.79, 127.4, 127.2, 126.8, 126.3, 122.5, 121.5, 121.0, 119.8, 118.6, 110.1, 100.9, 56.5, 56.0, 42.7, 41.1, 25.6, 20.8. IR (neat): ν 2969, 2926, 1737, 1597, 1491, 1437, 1365, 1229, 1217, 1207, 689 cm^{-1}. HRMS (ESI) calcd for $C_{24}H_{23}N_2$ (M+H): 339.1856. Found: 339.1850.

Product (3e)

1a + **2e** → **3e**

Reaction time: 40 h. Following the general procedure, tetrahydroisoquinoline **1a** (19.0 mg, 0.09 mmol) and indole **2e** (52.4 mg, 0.40 mmol) was converted to product **3e**[S6] (28.2 mg, 0.083 mmol) in 92% yield.
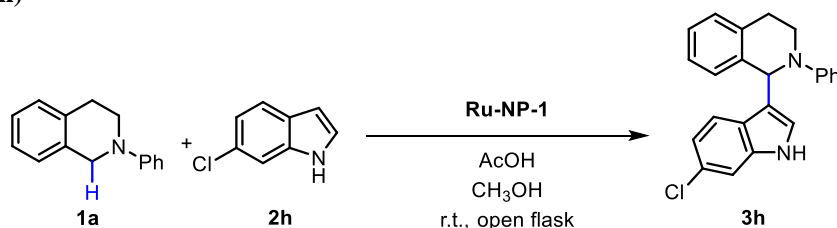
Product (3f)

Reaction time: 40 h. Following the general procedure, tetrahydroisoquinoline **1a** (21.0 mg, 0.10 mmol) and indole **2f** (58.8 mg, 0.40 mmol) was converted to product **3f**[S6] (29.1 mg, 0.082 mmol) in 82% yield.
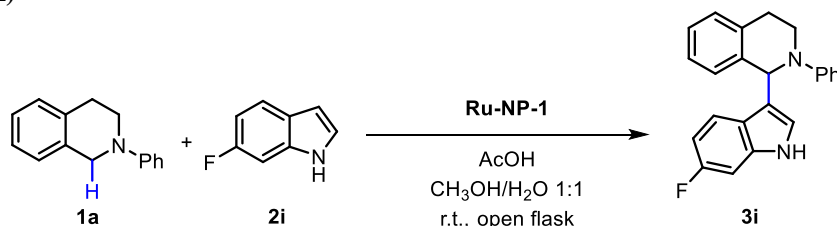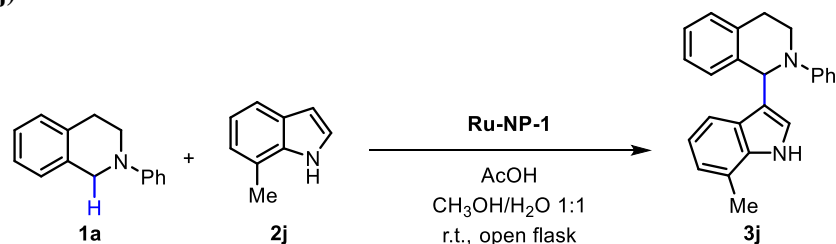
Product (3g)

Reaction time: 92 h. Following the general procedure, tetrahydroisoquinoline **1a** (20.9 mg, 0.10 mmol) and indole **2g** (52.4 mg, 0.40 mmol) was converted to product **3g**[S6] (22.5 mg, 0.067 mmol) in 67% yield.

Product (3h)

Reaction time: 96 h. Following the general procedure, tetrahydroisoquinoline **1a** (21.2 mg, 0.10 mmol) and indole **2h** (60.4 mg, 0.40 mmol) was converted to product **3h**[S6] (17.9 mg, 0.050 mmol) in 49% yield.

Product (3i)

Reaction time: 92 h. Following the general procedure, tetrahydroisoquinoline **1a** (20.9 mg, 0.10 mmol) and indole **2i** (52.4 mg, 0.40 mmol) was converted to product **3i** (33.6 mg, 0.098 mmol) in 98% yield.

3i: White solid: TLC R_f (10% EA/PE) = 0.18, mp = 161-163 °C. ^{1}H NMR (500 MHz, Acetone): δ 9.98 (s, 1H), 7.34 (dd, J = 8.3 and 5.8 Hz, 1H), 7.21 (d, J = 5.2 Hz, 1H), 7.08 − 6.90 (m, 8H), 6.66 − 6.50 (m, 3H), 6.11 (s, 1H), 3.57 − 3.40 (m, 2H), 2.91 (dt, J = 15.3 and 7.5 Hz, 1H), 2.76 − 2.70 (m, 1H). ^{13}C NMR (126 MHz, Acetone): δ 161.7, 159.3, 150.8, 138.6, 138.0 (d, J = 12.6 Hz), 136.3, 129.9, 129.6, 128.9, 127.5, 126.5, 126.1 (d, J = 3.4 Hz), 124.3, 121.6 (d, J = 10.1 Hz), 119.5, 118.8, 116.5, 108.1 (d, J = 24.4 Hz), 98.3, 98.0, 57.2, 42.9, 27.4. IR (neat): v 3425, 3015,
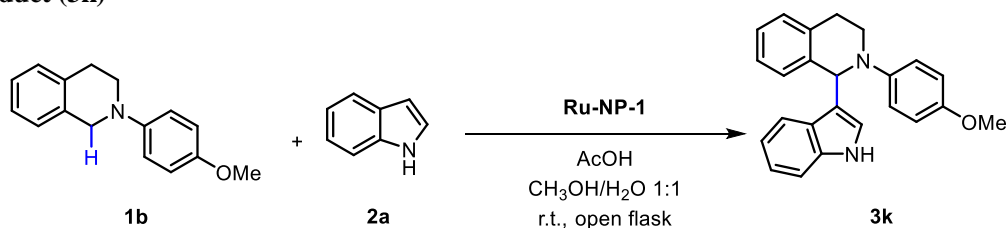
2942, 1736, 1598, 1364, 1215 cm^{-1}. HRMS (ESI) calcd for $C_{23}H_{20}FN_2$ (M+H): 343.1605. Found: 343.1610.

Product (3j)

Reaction time: 27 h. Following the general procedure, tetrahydroisoquinoline **1a** (20.9 mg, 0.10 mmol) and indole **2j** (52.4 mg, 0.40 mmol) was converted to product **3j**[S6] (23.8 mg, 0.070 mmol) in 70% yield.
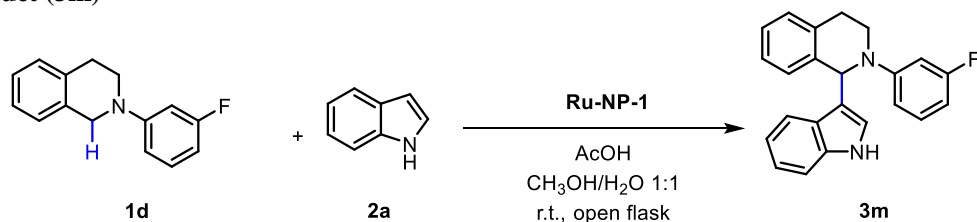
Product (3k)

Reaction time: 42 h. Following the general procedure, tetrahydroisoquinoline **1b** (11.8 mg, 0.05 mmol) and indole **2a** (23.4 mg, 0.20 mmol) was converted to product **3k**[S6] (10.1 mg, 0.029 mmol) in 58% yield.

Product (3l)
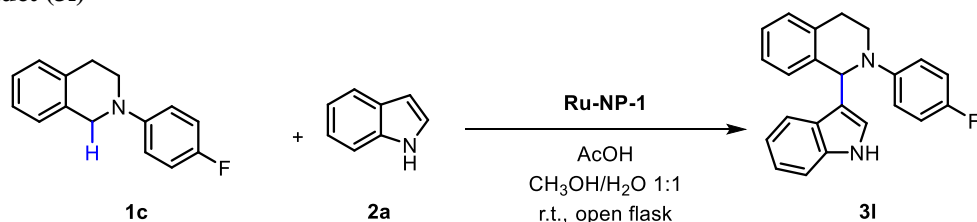
Reaction time: 42 h. Following the general procedure, tetrahydroisoquinoline **1c** (22.7 mg, 0.10 mmol) and indole **2a** (46.8 mg, 0.40 mmol) was converted to product **3l**[S6] (29.6 mg, 0.087 mmol) in 87% yield.
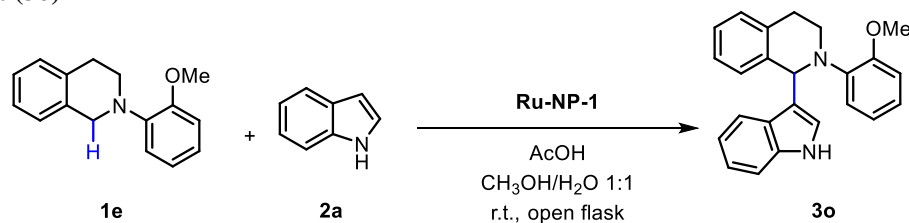
Product (3m)

Reaction time: 110 h. Following the general procedure, tetrahydroisoquinoline **1d** (20.6 mg, 0.09 mmol) and indole **2a** (46.8 mg, 0.40 mmol) was converted to product **3m** (27.4 mg, 0.080 mmol) in 80% yield. Recovered 10% of **1d** (2.1 mg, 0.006 mmol), 88% of yield (brsm), brsm = base on the recovered starting material.

3m: White solid: TLC R_f (10% EA/PE) = 0.17, mp = 165-167 °C. ^{1}H NMR (500 MHz, Acetone): δ 10.05 (s, 1H), 7.58 (d, J = 8.0 Hz, 1H), 7.46 – 7.40 (m, 1H), 7.37 (d, J = 8.2 Hz, 1H), 7.22 – 7.12 (m, 4H), 7.12 – 7.05 (m, 1H), 6.99 – 6.93 (m, 1H), 6.87 (dd, J = 8.4 and 2.3 Hz, 1H), 6.84 (dd, J = 2.4 and 0.7 Hz, 1H), 6.78 (dt, J = 13.2 and 2.4 Hz, 1H), 6.44 – 6.36 (m, 1H), 6.30 (s, 1H), 3.73 – 3.60 (m, 2H), 3.14 – 3.03 (m, 1H), 2.92 (dt, J = 16.2 and 5.1 Hz, 1H). ^{13}C NMR (126 MHz, Acetone): δ 166.0, 164.1, 152.4 (d, J = 10.5 Hz), 138.6, 138.1, 136.2, 131.2 (d, J = 10.3 Hz),

129.4, 128.8, 127.4 (d, J = 35.3 Hz), 126.6, 125.3, 122.4, 120.4, 119.8, 118.9, 112.3, 111.2 (d, J = 2.1 Hz), 104.1 (d, J = 21.7 Hz), 102.0 (d, J = 25.7 Hz), 57.1, 43.0, 27.5. IR (neat): v 3410, 3019, 2928, 1745, 1612, 1490, 1365, 1214, 739 cm^{-1}. HRMS (ESI) calcd for $C_{23}H_{20}FN_2$ (M+H): 343.1605. Found: 343.1605.
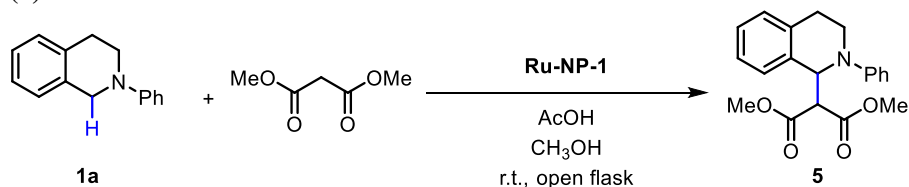
Product (3o)

Reaction time: 65 h. Following the general procedure, tetrahydroisoquinoline **1e** (36.8 mg, 0.15 mmol) and indole **2a** (46.8 mg, 0.40 mmol) was converted to product **3o**[S6] (22.2 mg, 0.080 mmol) in 41% yield.

Product (4a)
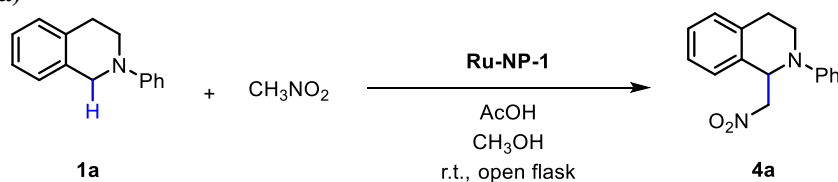
Reaction time: 36 h. Following the general procedure, tetrahydroisoquinoline **1a** (10.3 mg, 0.05 mmol) and nitromethane (12.2 mg, 0.20 mmol) was converted to product **4a**[S6] in 97% yield determined by ^{1}H NMR using 4-chloroacetophenone as an internal standard.
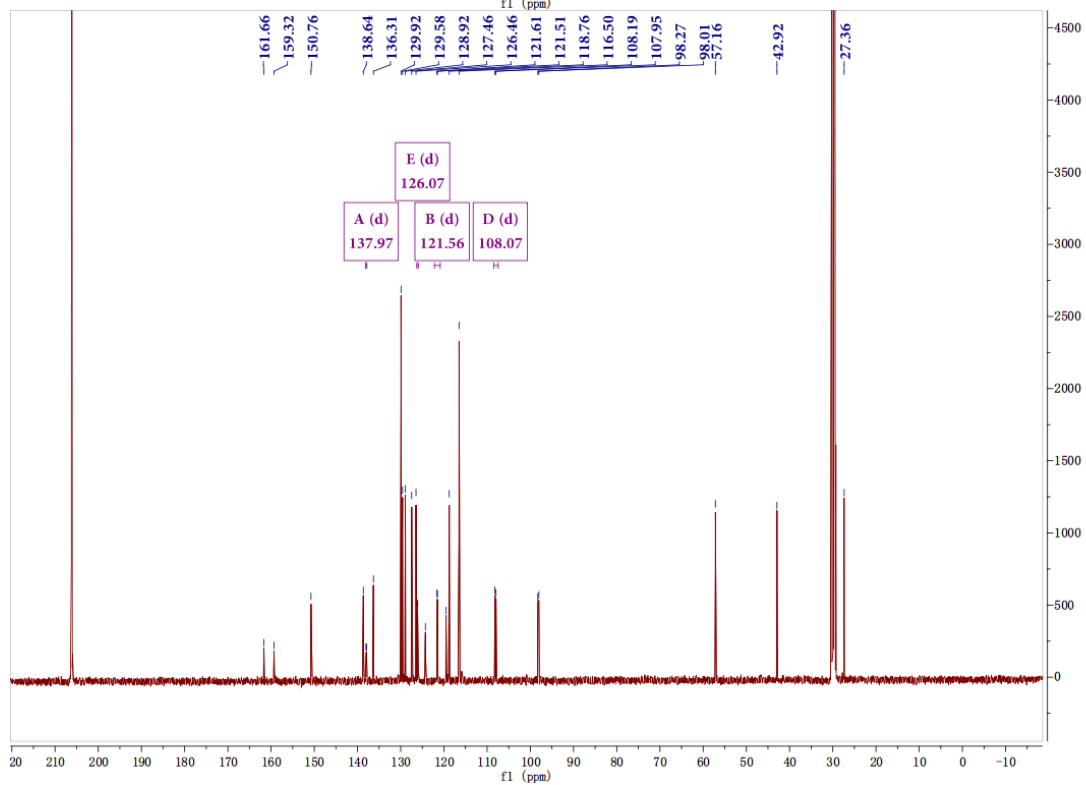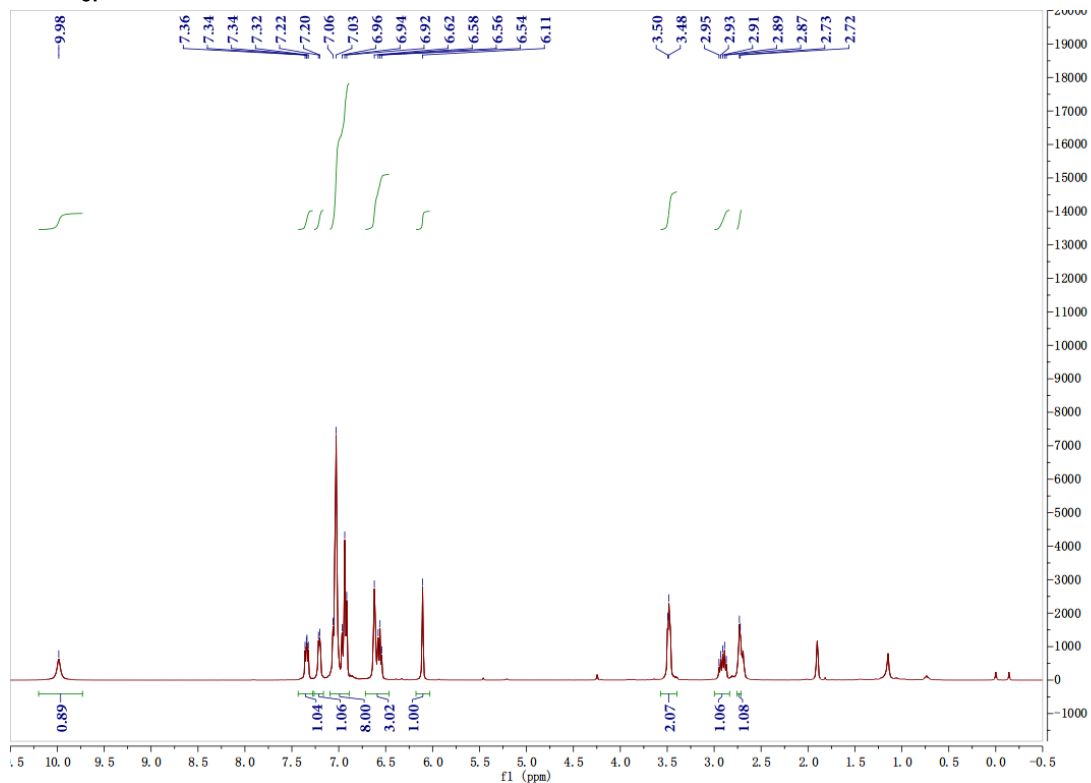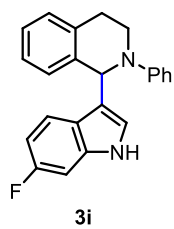
Product (5)

Reaction time: 46 h. Following the general procedure, tetrahydroisoquinoline **1a** (10.3 mg, 0.05 mmol) and dimethyl malonate (26.4 mg, 0.20 mmol) was converted to product **5**[S6] in 81% yield determined by ^{1}H NMR using 4-chloroacetophenone as an internal standard.

2.8 ^{1}H and ^{13}C-NMR spectra for new compounds

3d

3i

3m
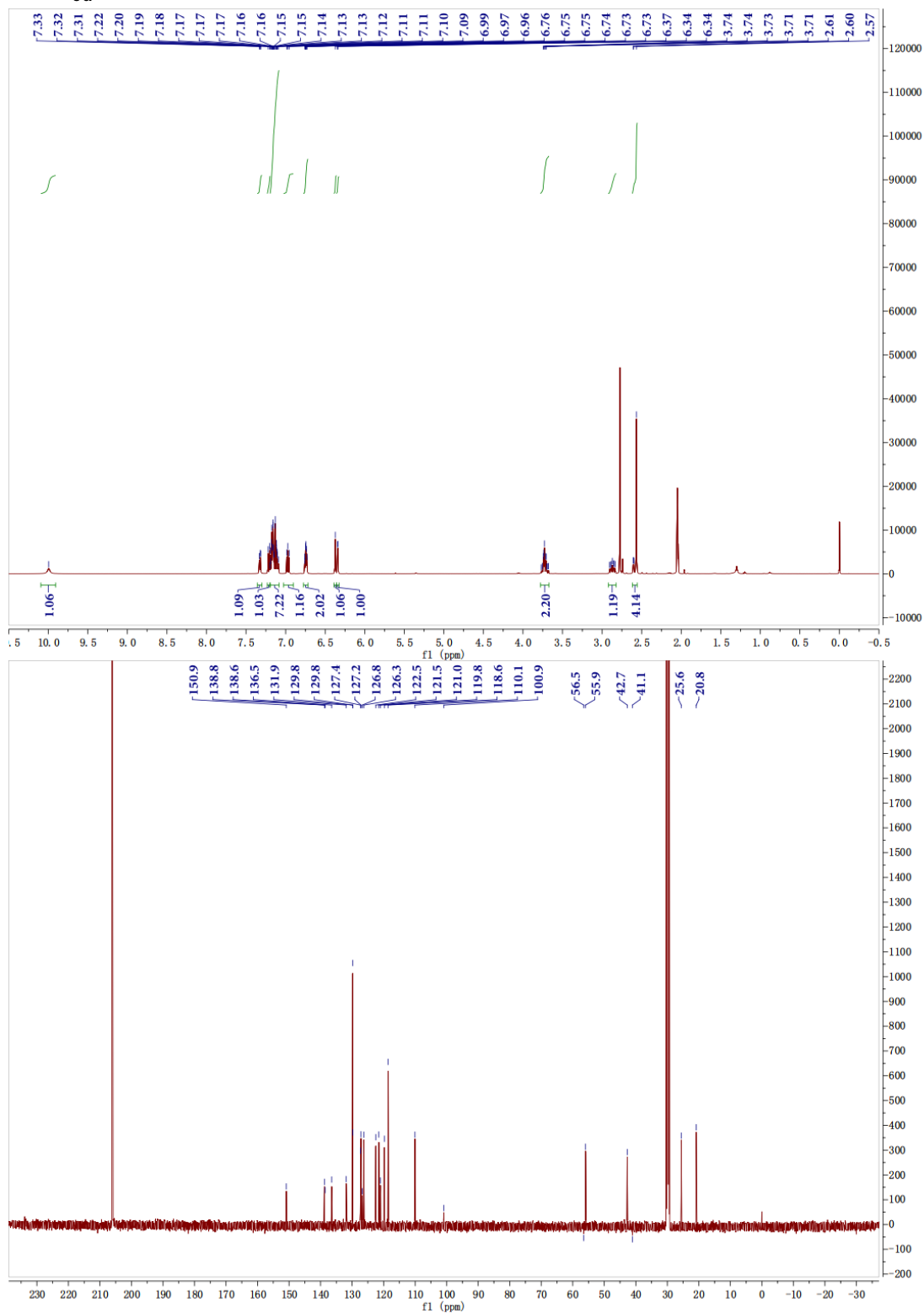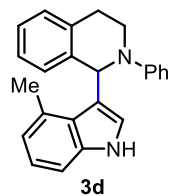
References

(S1) Zhong, J.-J.; Meng, Q.-Y.; Wang, G.-X.; Liu, Q.; Chen, B.; Feng, K.; Tung, C.-H.; Wu, L.-Z. *Chem. Eur. J.*, 2013, **19**, 6443.

(S2) Meanwhile, another work by Tokuyama and his co-workers also used AcOH for this reation. Ueda, H.; Yoshida, K.; Tokuyama, H. *Org. Lett.*, 2014, **16**, 4194.

(S3) Freeman, D. B., Furst, L., Condie, A. G., Stephenson, C. R. J. *Org. Lett.* 2012, **14,** 94.

(S4) Rueping, M., Vila, C., Koenigs, R. M., Poscharny, K., Fabry, D. C. *Chem. Commun.* 2011, **47**, 2360.

(S5) Clément, J.-L.; Ferré, N.; Siri, D.; Karoui, H.; Rockenbauer, A.; Tordo, P. *J. Org. Chem.* 2005, **70**, 1198.

(S6) Meng, Q.Y.; Zhong, J.-J.; Liu, Q.; Gao, X.-W.; Zhang, H.-H.; Lei, T.; Li, Z.-J.; Feng, K.; Chen, B.; Tung, C.-H.; Wu, L.-Z. *J. Am. Chem. Soc.* 2013, **135**, 19052.

(S7) (a) Gonza Condie, A. G.; González-Gómez, J. G.; Stephenson, C. R. J. *J. Am. Soc. Chem.* **2010**, *132*, 1464. (b) Freeman, D. B.; Furst, L.; Condie, A. G.; Stephenson, C. R. J. *Org. Lett.* **2012**, *14*, 94.

(S8) For selective reviews, see: (a) Li, C.-J. *Acc. Chem. Res.* **2009**, *42*, 335. (b) Yeung, C. S.; Dong, V. M. *Chem. Rev.* **2011**, *111*, 1215. (c) Girarad, S. A.; Knauver, T.; Li, C.-J. *Angew. Chem. Int. Ed.* **2014**, *53*, 74. (d) Girard, S. A.; Knauber, T.; Li, C.-J. *Angew. Chem. Int. Ed.* **2014**, *53*, 74. For selective reports, see: (e) Li, Z.; Li, C.-J. *J. Am. Chem. Soc.* **2005**, *127*, 6968. (f) Boess, E.; Schmitz, C.; Klussmann, M. *J. Am. Chem. Soc.* **2012**, *134*, 5317. (g) Ratnikov, M. O.; Xu, X.; Doyle, M. P. *J. Am. Chem. Soc.* **2013**, *135*, 9475. (h) Meng, Q.Y.; Zhong, J.-J.; Liu, Q.; Gao, X.-W.; Zhang, H.-H.; Lei, T.; Li, Z.-J.; Feng, K.; Chen, B.; Tung, C.-H.; Wu, L.-Z. *J. Am. Chem. Soc.* **2013**, *135*, 19052. (i) Nobuta, T.; Tada, N.; Fujiya, A.; Kariya, A.; Miura, T.; Itoh, A. *Org. Lett.* **2013**, *15*, 574. (j) Ueda, H.; Yoshida, K.; Tokuyama, H. *Org. Lett.* **2014**, *16*, 4194. (k) Tanoue, A.; Yoo, W.-J.; Kobayashi, S. *Org. Lett.* **2014**, *16*, 2346. (l) Wu, C.-J.; Zhong, J.-J.; Meng, Q.-Y.; Lei, T.; Gao, X.-W.; Tung, C.-H.; Wu, L.-Z. *Org. Lett.* **2015**, *17*, 884.

(S9) For selective reviews, see: (a) Schlögl, R.; Hamid, S. B. A. *Angew. Chem. Int. Ed.* **2004**, *43*, 1628. (b) Astruc, D.; Lu, F.; Aranzaes, J. R. *Angew. Chem. Int. Ed.* **2005**, *44*, 7852. (c) Lee, I.; Delbecq, F.; Morales, R.; Albiter, M. A.; Zaera, F. *Nat. Mater.* **2009**, *8*, 132. (d) Polshettiwar, V.; Varma, R. S. *Green Chem.* **2010**, *12*, 743. (e) Zahmakıran, M.; Özkar, S. *Nanoscale* **2011**, *3*, 3462. (f) Chng, L. L.; Erathodiyil, N.; Ying, J. Y. *Acc. Chem. Res.* **2013**, *46*, 1825.

(S10) (a) Tian, N.; Zhou, Z.-Y.; Sun, S.-G.; Ding, Y.; Wang, Z. L. *Science* **2007**, *316*, 732. (b) Zhang, X.; Corma, A. *Angew. Chem. Int. Ed.* **2008**, *47*, 4358. (c) Yang, J.; Sargent, E., Kelley, S., Ying, J. Y. *Nat. Mater.* **2009**, *8*, 683. (d) Witham, C. A.; Huang, W.; Tsung, C.-K.; Kuhn, J. N.; Somorjai, G. A.; Toste, F. D. *Nat. Chem.* **2010**, *2*, 36. (e) Yamada, Y.; Tsung, C.-K.; Huang, W.; Huo, Z.; Habas, S. E.; Soejima, T.; Aliaga, C. E.; Somorjai, G. A.; Yang, P. *Nat. Chem.* **2011**, *3*, 372. (f) Kesavan, L.; Tiruvalam, R.; Ab Rahim, M. H.; Saiman, M. I. B.; Enache, D. I.; Jenkins, R. L.; Dimitratos, N.; Lopez-Sanchez, J. A.; Taylor, S. H.; Knight, D. W.; Kiely, C. J.; Hutchings, G. J. *Science* **2011,** *331*, 195. (g) Crespo-Quesada, M.; Yarulin, A.; Jin, M.; Xia, Y.; Kiwi-Minker, L. *J. Am. Chem. Soc.* **2011**, *133*, 12787. (h) Wu, Y.; Cai, S.; Wang, D.; He, W.; Li, Y. *J. Am. Chem. Soc.* **2012**, *134*, 8975. (i) Kyriakou, G.; Boucher, M. B.; Jewell, A. D.; Lewis, E. A.; Lawton, T. J.; Baber, A. E.; Tierney, H. L.; Flytzani-Stephanopoulos, M.; Sykes, E. C. H. *Science* **2012**, *335*, 1209. (j) Li, Z.-X.; Xue, W.; Guan, B.-T.; Shi, F.-B.; Shi, Z.-J.; Jiang, H.; Yan, C.-H. *Nanoscale* **2013**, *5*, 1213.